RESEARCH ARTICLE

Factors Driving Intensification of Pre-Monsoon Tropical Cyclones Over the Bay of Bengal: A Comparative Study of Cyclones Fani and Yaas

Pankaj Lal Sahu[1] · Sandeep Pattnaik[1] · Prasenjit Rath[2]

Abstract

This research paper investigates the factors responsible for tropical cyclones' intensification process, focusing on pre-monsoon cyclones Fani and Yaas. Using the WRF model, the study examines the dynamics and thermodynamics of the two cyclones in three phases: pre-intensification, intensification, and post-intensification. The results are compared with available satellite data sets and it was found that Fani had higher wind speeds and a more structured system with high specific humidity concentrations closer to the storm center than Yaas. Before the RI of Fani, there was a sudden increase in moisture convergence rate, hydrometeors, and diabatic heating, facilitating the formation of cloud ice at the upper level of the troposphere and the release of higher latent heat energy. In contrast, the lack of moisture convergence in Yaas resulted in a weaker updraft and reduced latent heat release. Further analysis suggests that the heating in Fani was more intense and widespread in the inner eyewall region than the core, compared to Yaas. In general, it is also noted that an enhanced bulk kinetic energy (BKE) is a clear indicator for intensification and during the intensification phase, sustained BKE production and moderate dissipation are evident. The latent heating budget parameters indicate a continuous accumulation of moisture with nearly constant moisture consumption during the intensification process. These features are more distinct for Fani compared to the Yaas. The study concludes that during RI, dynamical processes play a dominant role compared to thermodynamical processes.

Keywords Fani · Yaas · Rapid intensification · Intensification phase · Heating · Hydrometeors

Introduction

The Indian subcontinent is majorly associated with two cyclone seasons namely pre-monsoon (March-May) and post-monsoon seasons (October-December). Each year, four to five tropical cyclones (TCs) are observed to make landfall in the coastal region of the country surrounding the BoB (Duan et al., 2021). The low-lying delta, shallow bathymetry, and funnel-shaped coastline associated with a large number of river basins all contribute to the high

number of fatalities in this region (WMO 2008). Accurately determining the strength of a TC is a tough task that is dependent on a number of complex parameters, including wind shear, large-scale interactions, the dominant thermodynamic state, inner core dynamics, and their interactions. Radial distribution of SST also plays a very important role in defining the storm structure and characteristics (Rai et al., 2016; Rai & Pattnaik, 2018). Rapid intensification (RI) of a tropical cyclone refers to a sudden and significant increase in its maximum sustained winds (MSW) of at least 30 knots (15.4 m/s) within 24 h (Kaplan & DeMaria, 2003). In contrast to the open oceans, which exhibit negligible annual variations in RI counts, the coastal offshore regions situated within a distance of 400 km from the coastline exhibit a notable increase in RI events. Specifically, the RI count in these regions has tripled from 1980 to 2020 (Li et al., 2023). The majority of TCs, approximately 80–85%, experience the RI phase within the North Indian Ocean (NIO) basin. The rapid change in intensity observed in TCs is a complex issue that operates on multiple scales. Various factors contribute

✉ Sandeep Pattnaik
spt@iitbbs.ac.in

1 School of Earth, Ocean and Climate Sciences, Indian Institute of Technology Bhubaneswar Argul, Jatni, Khurda, Odisha 752050, India

2 School of Mechanical Sciences, Indian Institute of Technology Bhubaneswar, Jatni, Khurda, Odisha 752050, India

to the formation and development of tropical cyclones. These factors encompass both large-scale phenomena, such as oceanic conditions, wind shear, the influx of dry air, and the distance between the cyclone's genesis and the coastline (Lee et al., 2016; Kaplan et al., 2010, 2015), as well as microscale interactions within the cyclone's inner core, specifically pertaining to convective processes, boundary layer processes, and microphysical processes (Liu et al., 2017; Zhao et al., 2020). During RI, the structure of the tropical cyclone also changes. The storm's central pressure drops, and the eyewall, where the heaviest precipitation and strongest winds are located, becomes more compact and better organized. This can result in a dramatic increase in wind speed and storm surge, which can be particularly dangerous for coastal communities. Hence, it can be inferred that the projected impact would be of a severe nature, emphasizing the need for increased focus on the study of inter-annual variability and the prediction of RI of TCs (Rappaport et al., 2012; Ito, 2016). However, the precise forecasting of rapid intensification (RI) in tropical cyclones has proven to be a significant challenge in recent years, primarily due to the shortcomings of forecasting models, imperfect initial conditions, and inherent predictability limitations(Li et al.,2023; Cangialosi et al.,2020).

The use of HWRF simulations and the CloudSat measurements yields high-resolution datasets related to ice water content, these datasets offer valuable insights into the intricate connection between ice water content and the rate at which tropical cyclones intensify. Recent findings indicate that TCs that undergo RI show a greater ice water content compared to TCs that intensify at a slower rate (Wu et al., 2020). The study reveals a strong positive correlation of over 0.8 between the latent heat release (LHR) and precipitated hydrometeors, namely rainwater, snow, and graupel. This correlation is notably higher when compared to

non-precipitated hydrometeors (cloud ice and cloud water). During the RI phase, the eyewall region experiences a saturation state, with relative humidity (RH) reaching approximately 100%. This high humidity level in the presence of maximum cloud water below the freezing level, suggests an increased occurrence of condensation and a restricted rate of evaporation (Nekkkali et al., 2022). In order to comprehend the intensification and structure formation of TC, it is necessary to establish a correlation between kinetic energy (KE) and latent energy (LE). The moist air originating from the planetary boundary layer (PBL) ascends and undergoes condensation, thereby releasing latent heat during this transformation. An intermediate phase stores released latent energy (LE) as total potential energy (TPE), resulting in lowering pressure. The analysis of volume-integrated bulk energetics reveals contrasting trends between BKE and BLE as the cyclone intensifies and enters the bulk-energetically growing stage (Baisya et al., 2020).

The main aim of this study is to gain insight into the factors that contribute to the intensification process of pre-monsoon TC in the Bay of Bengal (BoB) region by using a high-resolution numerical model forecasts. Specifically, with thrust on the characterization of intensification phases (including pre and post phases) and investigate the dominant physical and thermodynamic processes associated with the same. The paper is structured as follows: it begins with an introduction (Section Introduction), followed by a description of the model and methodology (Section Model and Methodology), results and discussions (Section Results and Discussions), and conclusions (Section Summary).

Model and Methodology

Model

The Weather Research and Forecasting (WRF) model has been extensively used to forecast cyclones in the North Indian Ocean (NIO). The WRF model is employed as one of the systems in the operational forecasting process by the India Meteorological Department (IMD). Two TCs over the NIO/BoB region that saw noticeable intensity changes are examined using the WRF model. They are Fani and Yaas. The model integration begins at 1200 UTC on April 27, 2019, and concludes at 1200 UTC on May 2, 2019, for the Fani. Similarly, for the Yaas begins at 0000 UTC on May 23, 2021, and concludes at 0000 UTC on May 27, 2021.

The physical parameterization schemes listed in Table 1 are more suitable for the NIO basin (Vishwakarma & Pattnaik, 2022; Trivedi et al., 2023). The model's microphysical processes are simulated using the WRF double-moment six-class (WDM6) scheme. It is the extended

Table 1 WRF model configuration details

WRF-ARW version	4.0
Domains	Parent domain (9 km) with nested domain (3 km)
Time integration	30 s
Vertical levels	53 (Top level 50 hPa)
Initial and boundary condition	GDAS 0.25×0.25
SST Update	ERA5 (6 hourly)
Model Physics	
Longwave Radiation	RRTM (Mlawer et al., 1997)
Shortwave Radiation	Dudhia (Dudhia, 1989)
Microphysics	WDM6 (Lim et al. 2010)
Surface physics	MM5 Similarity scheme (Paulson, 1970)
Cumulus	Kain Fritsch (Kain, 2004), 3 km Explicit
Planetary Boundary Layer	Yonsei University scheme (Hong et al., 2006)

version of the WSM6 scheme (Lim et al., 2010) which is used in the operational model at IMD for the NIO basin. According to Chakraborty et al. (2021), the WDM6 microphysical scheme demonstrates better predictive capabilities for frozen hydrometeors, enabling a more accurate presentation of the cold rain process. These forecasts used initial and boundary conditions obtained from the NCEP Global Data Assimilation System (GDAS) at a resolution of 0.25° x 0.25°, and the boundary conditions were updated every six hours in accordance with the GDAS forecasts (NCEP, 2015). The SST updates were obtained from ERA5 reanalysis data at 6-hour intervals (Hersbach et al., 2023). The best track data from the IMD are used to compare model-simulated track positions, minimum sea-level pressure (MSLP), and maximum sustained wind (MSW) speed (available at www.rsmcnewdelhi.imd.gov.in). The total column cloud ice parameter from the Moderate Resolution Imaging Spectrometer (MODIS) was used for validation. All of the results shown are for the innermost domain (3 km).

Methodology

RI of a TC refers to a sudden and significant increase in its maximum sustained winds (MSW) of at least 30 knots (15.4 m/s) within 24 h (Kaplan & DeMaria, 2003). The following procedures are used to determine the composite or average structure in this analysis: Using the mean sea level pressure, the center of the forecasted TC is recorded at three-hour intervals from the innermost domain (D2). Subsequently, within each phase, namely 24 h prior to the commencement of the Intensification phase (IP -24), during the onset of the Intensification phase (IP), and 24 h following the Intensification phase (IP + 24), the region encompassing a 360×360 km area surrounding the storm's center is subjected to averaging. In other words, eight snapshots are averaged during each phase to derive the composite.

Using the equations proposed by Yanai et al. (1973), diabatic heating has been calculated from the model output:

$$s = c_p T + gz \qquad (1)$$

$$Q_1 = \frac{\partial \bar{s}}{\partial t} + \bar{v} \cdot \nabla \bar{s} + \omega \frac{\partial \bar{s}}{\partial p} \qquad (2)$$

$$Q_1 = Q_R + L(c - e) - \frac{\partial \overline{s'\omega'}}{\partial p} \qquad (3)$$

the variables used in the above equations: ω, T, c_p, e, c, Q_R, p, L, v, s, Q_1, z, and g respectively correspond to the following physical quantities: vertical wind speed, temperature, specific heat capacity of air at constant pressure, rate of re-evaporation of cloud droplets, rate of condensation per unit mass of air, radiative heating, pressure (hPa), latent heat of vaporisation of liquid water in (J/Kg), horizontal, wind speed (m/s), dry static energy, diabatic heating, altitude (m), acceleration due to gravity (9.8 m/s²) respectively. Variables denoted by a bar and a prime symbol represent the average and perturbation values, respectively, for the specific time period being analysed.

To calculate the quasi-Lagrangian budget using the energetic method the corresponding analysis is performed (Hogsett & Zhang, 2009; Baisya et al., 2020). For this analysis and budget calculation, the following parameters are used: The different variables employed are summarised as follows: universal gas constant (R), specific humidity (q_v), specific heat at constant volume (C_v), specific heat at constant pressure (C_p), pressure at a certain height (P), pressure at mean sea level (P_0), perturbation pressure (ṕ), latent heat of vaporisation (L_v), horizontal velocity (V_h), height (h), heating due to condensation (Q_c), gravitational acceleration (g), evaporative heating (Q_e), density of air (ρ), air temperature (T), natural logarithm (ln), volume (v), initial translational velocity of the control volume (V_1), and final translational velocity of the control volume (V_2):

Latent energy $(\mathrm{LE}) = \rho L_v q_v$,

Total potential energy (TPE) = potential energy + internal energy = $\rho g Z + \rho C_v T$,
   and
   Kinetic energy $(\mathrm{KE}) = \rho \frac{V_h \cdot V_h}{2}$

$$\begin{aligned} \frac{d(\mathrm{LE})}{dt} &= \text{Latent heat flux (LHF)} - \sigma L_v(Q_c - Q_e) + \mathrm{LE}\frac{d(\ln\rho)}{dt} \\ &= \mathrm{LHF} + \mathrm{LHR} + \mathrm{LDEN} \end{aligned} \qquad (4)$$

In the above equations, LHF represents the latent heat flux from the ocean surface, LHR refers to latent heat release, and LDEN represents the density-dependent variations in latent energy. The equation $L_v(Q_c\text{-}Q_e)$ represents the resultant heating rate and is expressed as $C_p/\pi\frac{d\theta}{dt}$, where $\pi = (P_0/P)^R/C_p$, and $\frac{d\theta}{dt} \sim \nabla\Theta \cdot (V_2 - V_1)$.

The change in the TPE can be expressed as

$$\begin{aligned} \frac{d(\mathrm{TPE})}{dt} &= \nabla \cdot (Pv) + V_h \cdot \nabla\dot{p} + \rho L_v(Q_c - Q_e) \\ &\quad + \mathrm{SHF} + \mathrm{TPE}\frac{d(\ln\rho)}{dt} \end{aligned} \qquad (5)$$

The first term on the right-hand side of the equation represents pressure convergence, followed by horizontal cross-isobaric flow. The variable p' denotes the pressure perturbation. The third, fourth, and fifth terms reflect LHR with the opposite sign, sensible heat flux from the ocean

surface, and condensation or dilution of TPE because of changes in density.

$$\frac{d(\text{KE})}{dt} = -V_{\text{h}} \cdot \nabla \dot{p} - V_{\text{h}} \cdot F + \text{KE}\frac{d(\ln \rho)}{dt} \tag{6}$$

The first term on the right-hand side of the equation represents KGEN, the work done by the air parcel against the pressure gradient force. The subsequent term represents KDIS, which indicates the dissipation of kinetic energy resulting from friction in boundary layer processes as well as vertical and horizontal diffusion. The third term represents KDEN, which refers to changes in kinetic energy caused by changes in density.

Using column-integrated and averaged quantities within a storm-relative framework allows the investigation of temporal variations in storm energetics within a control volume with $R = 180$ km and $z = 15$ km. As proposed by Dutton (1976), the volumetric expressions of the budget equations for kinetic energy and latent energy can be formulated as:

$$\frac{d(\text{BKE})}{dt} = -\int (V_{\text{h}} \cdot \nabla \dot{p})\, dv - \int (V_{\text{h}} \cdot F)\, dv \\ -\int \{\nabla \cdot \text{KE}\,(V_2 - V_1)\}\, dv \tag{7}$$

$$\frac{d(\text{BLE})}{dt} = -\int \{\sigma L_{\text{v}}\,(Q_{\text{c}} - Q_{\text{e}})\}\, dv - \int (\text{LHF}) dv \\ -\int \{\nabla \cdot \text{LE}\,(V_2 - V_1)\}\, dv \tag{8}$$

Results and Discussions

Tracks and Intensity

The observed best track and intensity from IMD and from the WRF model for the cyclones Fani (105 h) and Yaas (84 h), including the storm's dominant intensification phase are presented in Fig. 1. The simulated trajectory of Fani accurately reproduces its initial movement towards the northwest, followed by a subsequent eastward curvature that brings it in closer proximity to the IMD. However, in the case of TC Yaas, the simulated track showed a slight deviation from the IMD best track during the initial 12-hour period. However, as the forecast advanced, it successfully reproduced the track provided by the IMD. The discrepancy observed in the initial prediction for TC Yaas may be attributed to the model spin-up problem, which was less prominent in the case of TC Fani, a more well-structured tropical cyclone. Despite this slight deviation, the model adequately captured the projected paths for both tropical cyclones in comparison to the IMD and, of utmost significance, accurately replicated the

duration of intensification (which will be discussed in the following section). Hence, the forecast products generated by the model exhibit robustness and are well-suited for subsequent diagnostic analyses.

Figure 2(a, b) displays the TC intensity in relation to Maximum Sustained Wind (MSW) and Mean Sea Level Pressure (MSLP). In general, the simulated intensities of both tropical cyclones showed a tendency to overestimate by up to 35 knots (35 hPa) in terms of MSW (MSLP) across the entire forecast period. For Fani, the magnitude of RI for the model forecast (IMD) is 27 (30 kts, 29 Apr 03UTC − 30 Apr 03UTC, 24 h). Similarly, in the case of non-RI cyclone Yaas, the model (IMD) projected intensification is 15.45 (20 kts, 24 May 12UTC − 25 May 12UTC, 24 h). Hence it is evident that the model-generated forecast is able to capture the RI phase of the Fani, as noted in the IMD, with a margin of 3 kts. In addition, the intensification of VSCS Yaas suggested that the model is able to simulate the intensification phase by a margin of 5 kts as compared to IMD. Therefore, we have comprehensively analyzed these two storms obtained from the model data as RI (Fani) and non-RI (Yaas) cases. In the following section, the discussions are segregated into three themes of composite analysis, i.e. pre-intensification Phase (IP-24), Intensification phase (IP), and post-intensification phase (IP + 24). The IP for Fani is 29 Apr 03 UTC to 30 Apr 03 UTC, while for Yaas it is 24 May 12 UTC to 25 May 12 UTC.

Characterization of Intensification Phase

The 850 hPa wind speed of the RI cyclone (Fani) and non-RI Cyclone (Yaas) is shown in Fig. 3. It is noted that in both the cyclones, the maximum intensity is at the southeastern quadrant but in the case of Fani 24 h before intensification (Fig. 3a) the maximum wind speed was in the southern sector with a wind speed of up to 58 knots. In contrast, in the case of Yaas (Fig. 3d), the wind speed was very low (~ 16–24 knots) and nearly uniform around the vortex. During the intensification phase in the case of Fani (Fig. 3b), wind speed reached up to 88 knots and extended up to 60 km at the southeastern quadrant, while in Yaas, maximum wind speed (~ 76 knots) extended from the southeastern to southwestern quadrant. After the intensification phase (Fig. 3c), wind speed is maximum in the southeastern sector, with wind speed ranging up to 100 knots extending up to 100 km from the center. While in the case of Yaas (Fig. 3e), wind speed went up to 82 knots and extended up to 90 km from the center.

The MSLP (Fig. 4) in the case of both Fani and Yaas was nearly the same in before, during, and after IPs. The distribution pattern of SLP reveals that the cyclone Fani
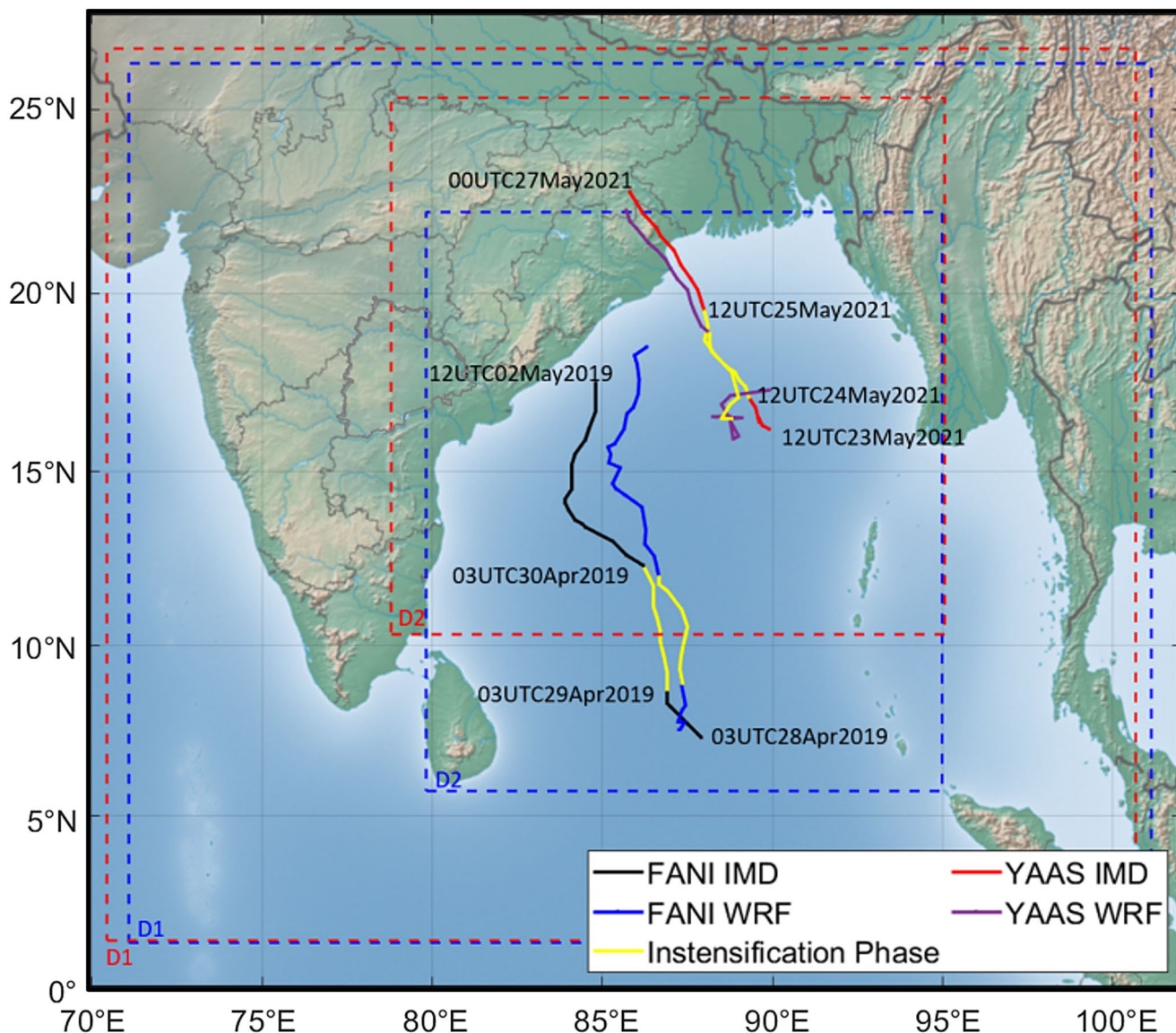
Fig. 1 Observed (IMD) and simulated storm tracks of Fani and Yaas. The blue dashed lines define the outer (D1) and inner (D2) WRF domain for Fani and the red dashed line for Yaas. Abbreviations: IMD, India Meteorological Department; WRF, Weather Research and Forecasting

and Yaas was a very organized system; its shape was circular and consistent. High specific humidity at 850 hPa in Fani is more concentrated near the center, while in Yaas, it is more widespread. Specific humidity is less in the south to the southwestern region in all the phases, and it increases up to 3 g/kg in the southwestern region during intensification on Fani. The high specific humidity ($\sim$ 17–20 g/kg) concentrated at a 30 km radius only before, during, and after the intensification phase in Fani, while in Yaas, moisture was nearly uniformly radially widespread around the center and did not show any specific structure. One of the reasons for the better spatial moisture structure in Fani might be due to better organization and severe intensification of the TC Fani.

Hydrometeors and Thermodynamics

Figure 5(a, b) illustrates the hydrometeors, including cloud ice, snow, cloud water, rainwater, and graupel, as well as diabatic heating, within a radius of 180 km from the center of the TC. Before the intensification phase, there was a notable increase in hydrometeors (excluding cloud water) and diabatic heating in the case of Fani. Rainwater, snow, and graupel showed a sharp (gradual) increase in Fani (Yaas), reaching up to 24 (15×10^{-5} kg/kg), 14 (7×10^{-5} kg/kg), and 9 (6.5×10^{-5} kg/kg), respectively, at the start of the intensification phase. This sharp increase contributes to Fani's rapid intensification, whilst the Yaas hydrometeors are pretty stagnant. At the beginning of IP, there is a drop in
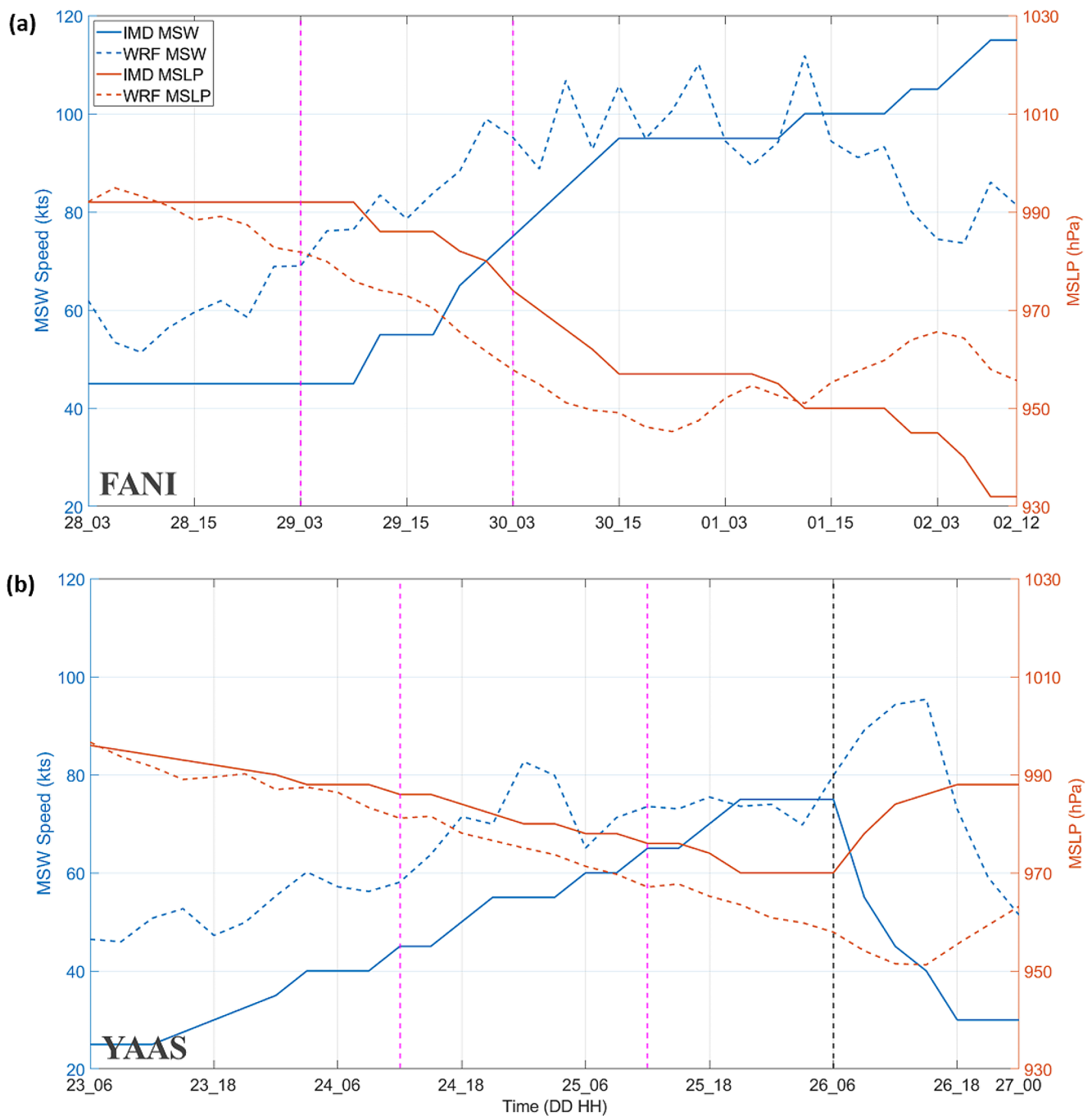
Fig. 2 The model simulated and observed intensity in terms of MSW speed (left axis) and MSLP (right axis) of cyclones (**a**) Fani and (**b**) Yaas. The vertical dashed magenta line shows the intensification phase, and the vertical dashed black line shows the landfall period. Abbreviations: IMD, India Meteorological Department; MSW, maximum sustained wind; MSLP, Minimum sea level pressure

cloud water and an increase in cloud ice, which may represent the transformation of cloud water into cloud ice, as seen in Fig. 5a, caused by the release of latent heat. The expansion of cloud water above the freezing level (0ºC isotherm at 550–500 hPa) may account for the increase of frozen hydrometeors (Nekkali et al., 2022). Clearly, the rise in diabatic heating from 0.7 K/hr to 2.3 K/hr during RI has had a major part in the intensification of Fani, but for Yaas the increase is just from 0.6 K/hr to 1.6 K/hr.

Further, a cross-section analysis is done from Fig. 6; it can be noted that in the case of both Fani and Yaas, Frozen hydrometeors, liquid hydrometeors, and diabatic heating are more in the western side of the cyclone. The anomalous structure of frozen and liquid hydrometeors are quite
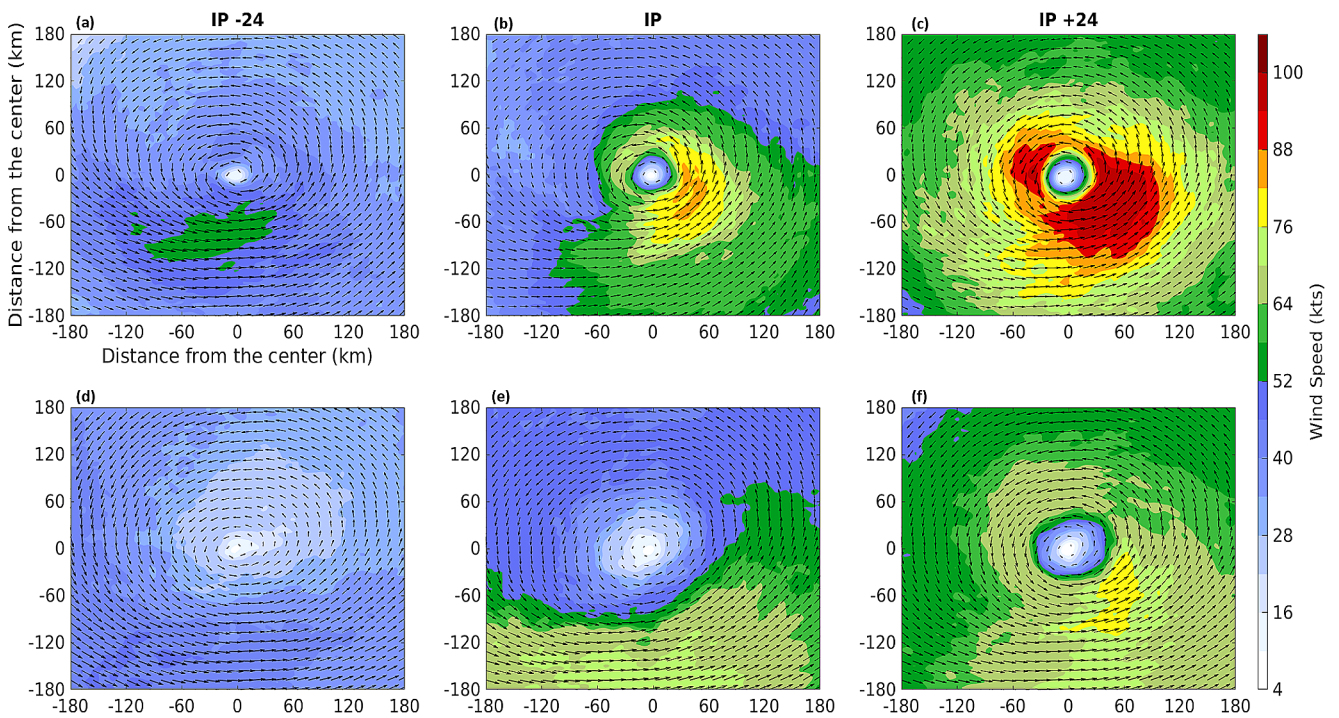
Fig. 3 Time average 850 hPa wind speed (kts) and wind direction before (**a**), during (**b**) and after IP (**c**) for Fani. (**d–f**) are the same as (**a–c**) but for Yaas (second row). Abbreviations: IP, Intensification Phase
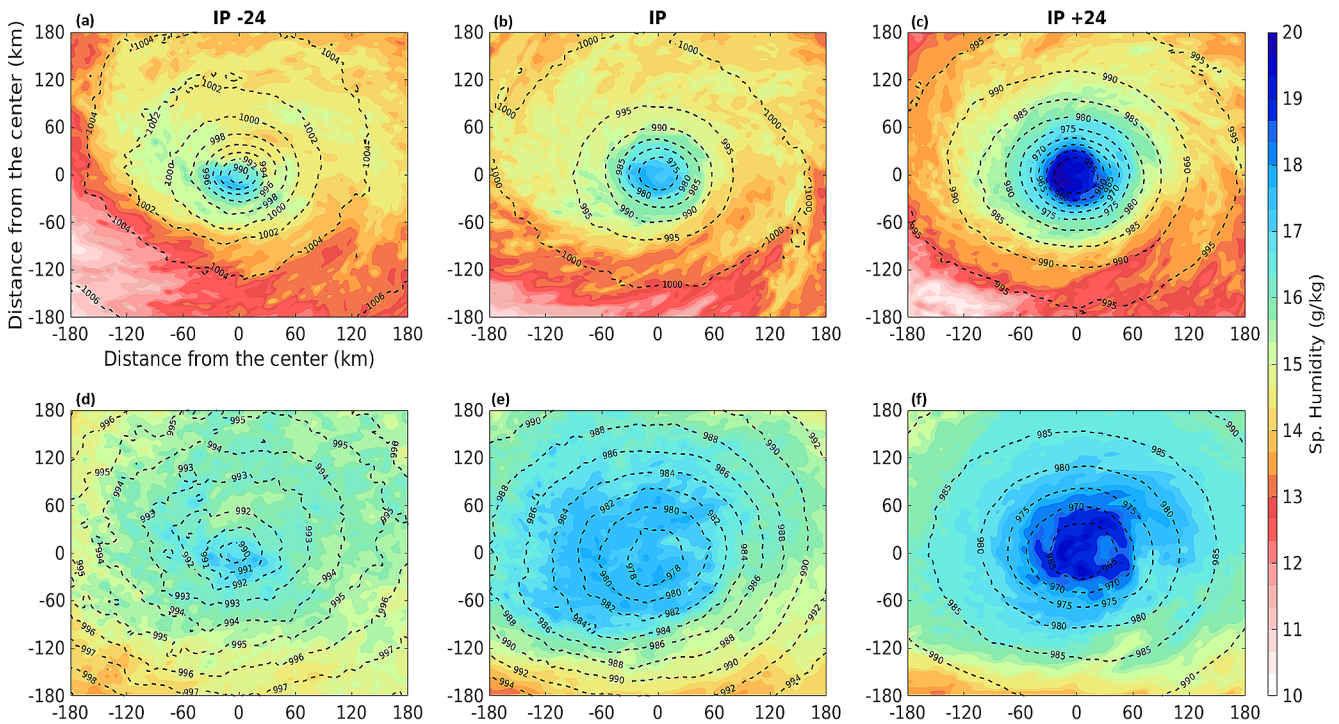

Fig. 4 Time average 850 hPa specific humidity (g/kg) (shaded) and MSLP (hPa) (contour) before (**a**), during (**b**) and after IP (**c**) for Fani. (**d–f**) are the same as (**a–c**) but for Yaas (second row). Abbreviations: IP, Intensification Phase; MSLP, Minimum sea level pressure
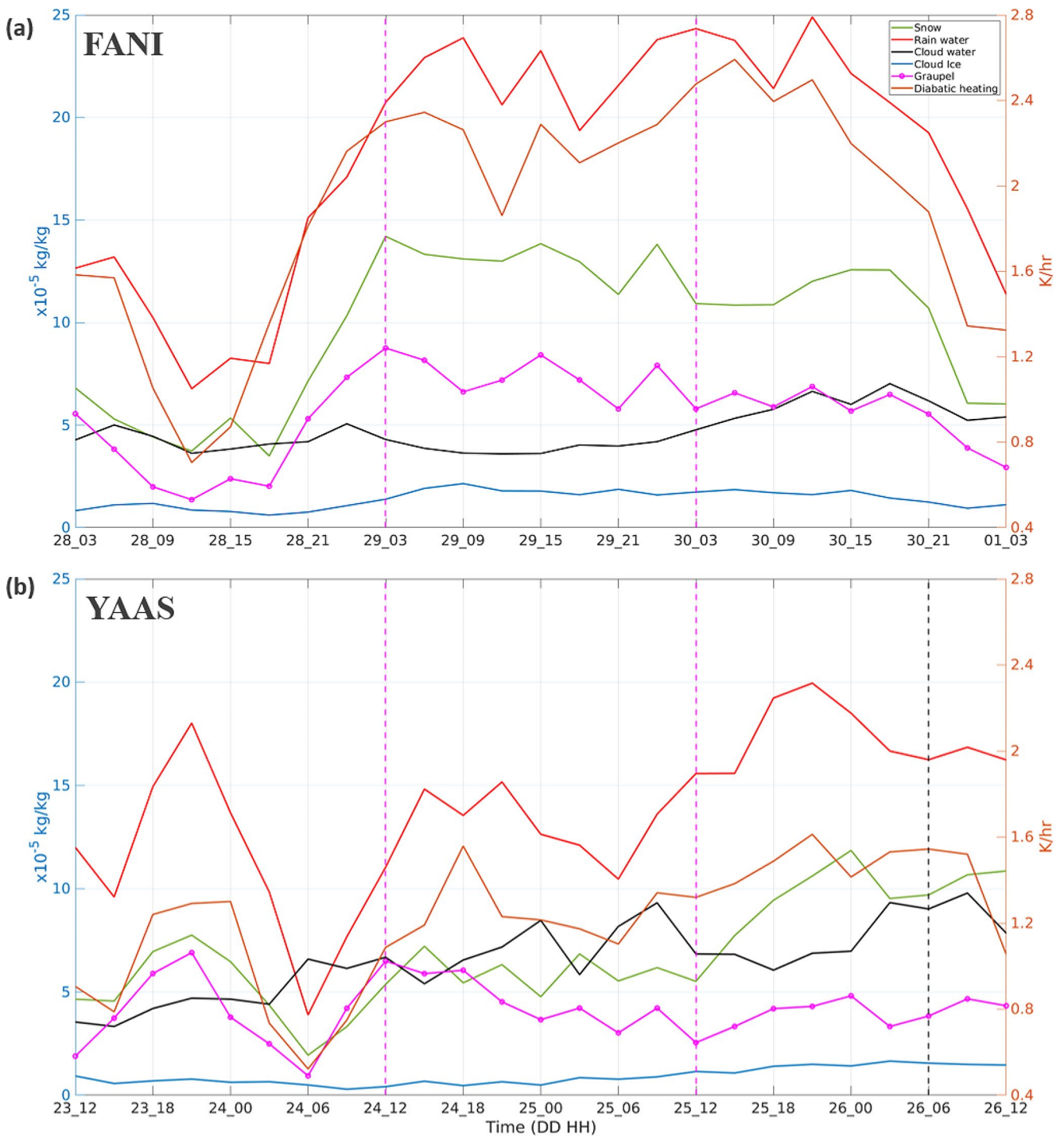
Fig. 5 Time series of hydrometeors (kg/kg) (left side) and diabatic heating (K/hr) (right side) for (**a**) Fani and (**b**) Yaas. The vertical dashed magenta line shows the intensification phase, and the vertical dashed black line shows the landfall period

similar before, during, and after the intensification phase of Fani. While in the case of Yaas, there is a huge amount of frozen hydrometeors around 140 km west before IP, during IP concentration of frozen hydrometeors reduced relative to the core region, and after IP, frozen hydrometeors concentration further shifted towards the center by

nearly 30 km from the center while liquid hydrometeors structure is quite similar in all the phases. The main difference in both the cyclones is in case Fani hydrometeors concentration is higher in the eyewall region than the core region. The reason might be the condensation and freezing of huge amounts of hydrometeors near the eyewall
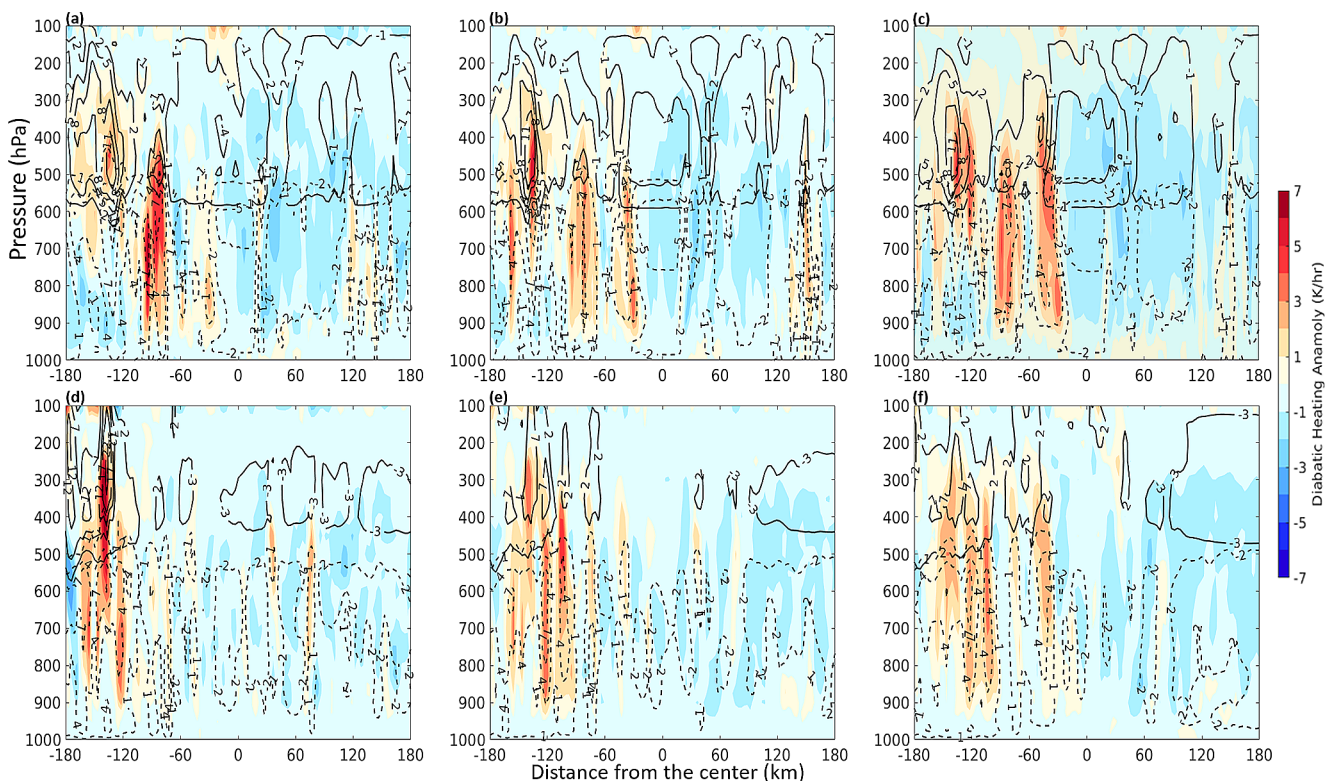
Fig. 6 Time average anomaly of diabatic heating (K/hr) in shading, frozen hydrometeors (kg/kg) in solid contour and liquid hydrometeors (kg/kg) in dashed contour for Fani (**a**) IP-24, (**b**) IP and (**c**) IP+24 and same for Yaas in (**d-f**) respectively

region; releasing heat during the microphysical process helps the intensification of Fani. As noted in the case of Fani, the heating is more at the 60 to 120 km region before IP, and it extended from 900 hPa to 400 hPa (lower to mid levels) in the 30 to 120 km region and 700 to 300 hPa in 120 to 150 km region during and after IP respectively (Fig. 6a-c). While in the case of Yaas, the heating was higher in 600 to 200 hPa (middle to upper levels) in the 120 to 150 km region before IP and during and after IP; it extended toward the center but not much heating with respect to the core region (Fig. 6d-f).

The satellite validation of the total column of cloud ice from Modis Aqua (Fig. 7) shows the precise location with model cloud ice for both Fani and Yaas. However, the model underestimates the cloud ice. In the case of Fani IP-24 (Fig. 7a, c), cloud ice is nearly 18 g/m^2, and for IP+24, it is nearly 15 g/m^2 for WRF (Fig. 7b), while about 24 g/m^2 for Modis Aqua (Fig. 7d), for IP satellite data was not available for validation. In the case of Yaas at IP-24 ((Fig. 7e, h) WRF underestimated the cloud ice, and in IP and IP+24, it is nearly the same.

Moisture Budget

In Fig. 8, the hourly rain rate and evaporation rate are depicted alongside the various moisture budget equation

terms in order to better comprehend the rain rate and evaporation relationship with the moisture convergence at various intensification phases. The Moisture Flux Convergence (MFC) has been computed according to the approach used by Banacos et al. (2005). MFC is consistent with the rain rate for both cyclones, the advection term contributes negatively, and the local term is negligible compared to the convergence and advection terms. The evaporation rate is also negligible compared to the rainfall rate. Nearly 12 h prior to Fani's RI, the moisture convergence rate increased to 0.8 s^{-1}; as shown in Fig. 5a, the rapid rise in moisture convergence resulted in the formation of considerably more cloud ice and the release of more latent heat energy. However, lack of moisture convergence in the case of Yaas resulted in a weaker updraft and thus resulted in lesser liquid hydrometeors transportation to the upper level and a decrease in latent heat release. The increase in cloud water, decrease in graupel, and nearly constant snow and cloud ice during the IP of Yaas indicate a lack of cloud water transport to the upper level; consequently, the simulated precipitation was primarily due to the warm rain process. After the RI period in the case of Fani, MFC decreased so that the rain rate and frozen hydrometeors too, which shows a high moisture convergence rate is needed for RI of the TC.
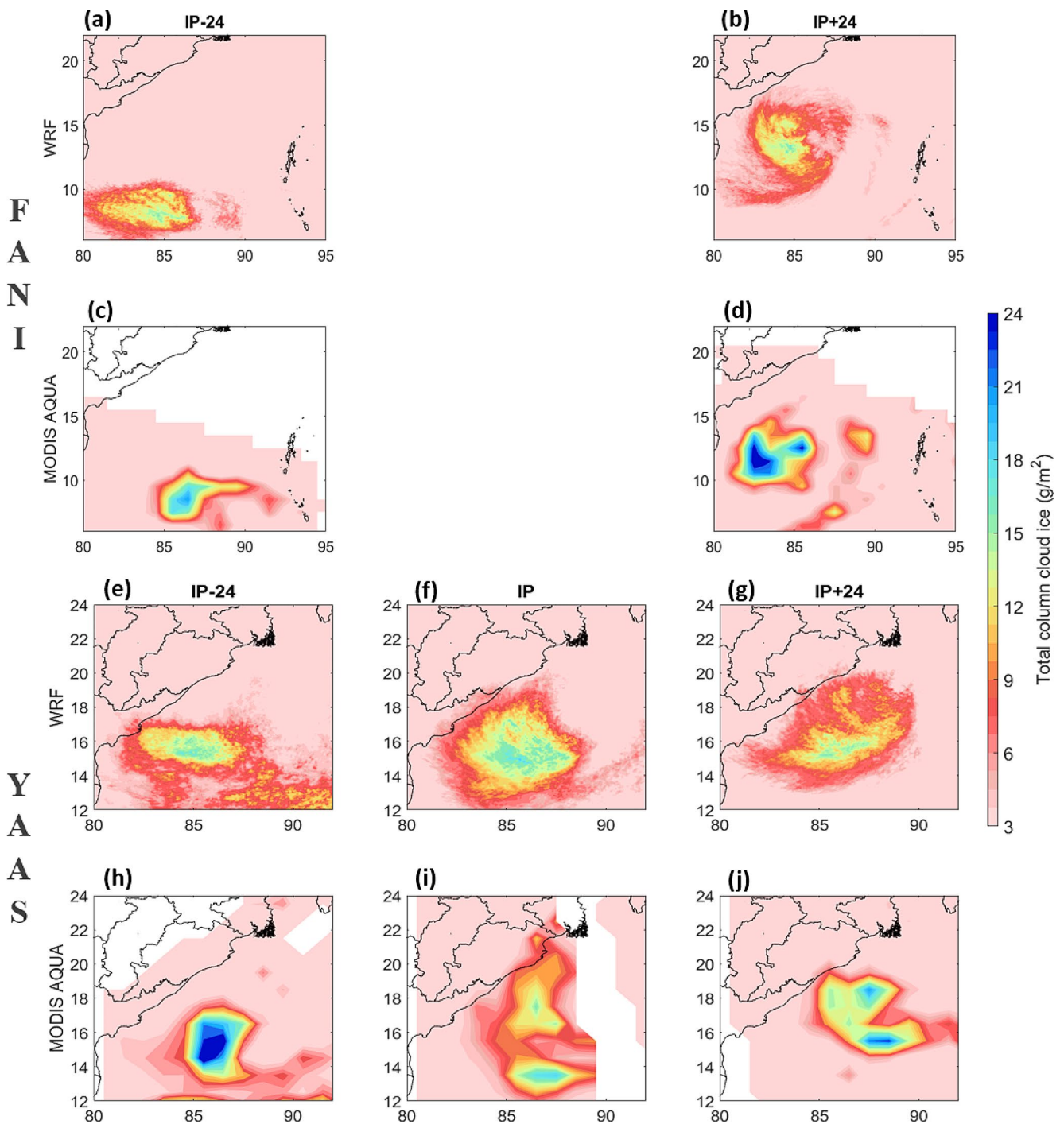
Fig. 7 Satellite validation of cloud ice from WRF model output (**a, b**) with MODIS AQUA (**c, d**) for Fani, same for Yaas in (**e-j**)

Storm Energetics

The time series of volume-integrated BKE (red), BTPE (blue), and BLE (black) is shown in Fig. 9(a-e). In order to set zero as the reference point, the obtained results are normalized relative to the initial value noted at the 12-hour of the forecast, following the spin-up period. The change in

BKE is in reasonable coincidence with the intensity change (Fig. 9(a, e) and 2(a, b)). For the Fani case, it is observed that there exists a clear and pronounced increasing trend in BKE (approximately occurring prior to 6 h of RI) in contrast to BTPE, where a slight increase is observed, followed by a subsequent decline in BLE. However, from 30_21 onwards, the BKE has exhibited a notable increase of approximately $0.32 \, \text{J} \cdot \text{m}^{-3}$, while concurrently displaying a declining trend
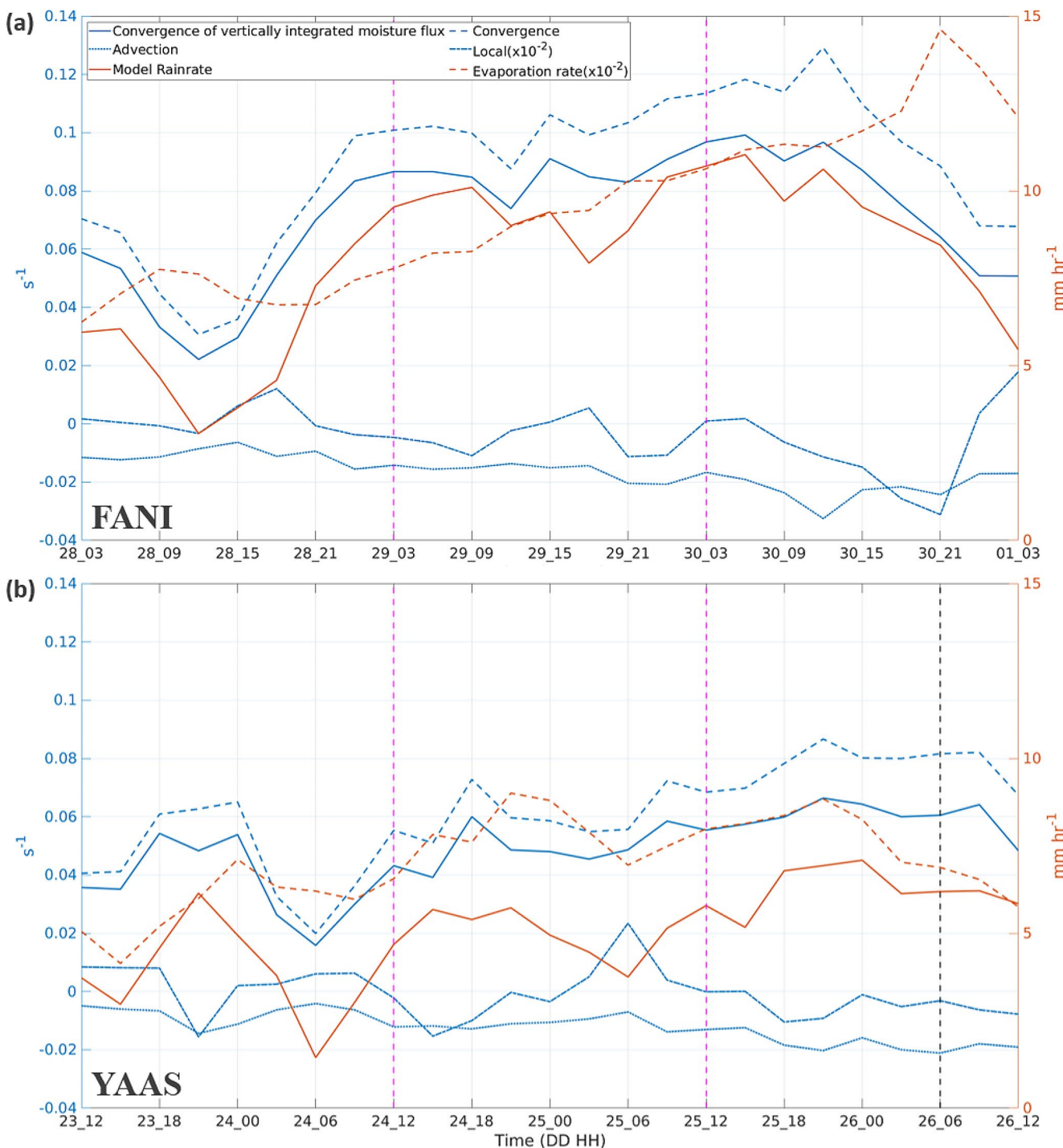
Fig. 8 Time series of moisture budget with convergence, advection, and local term (s^{-1}) (left side), model rain rate and evaporation rate (mm hr^{-1}) (right side) of moisture budget for (**a**) Fani and (**b**) Yaas. The vertical dashed magenta line shows the intensification phase, and the vertical dashed black line shows the landfall period

in BTPE. These observations imply that the rapid inward flow has played a crucial role in the intensification of the storm, at the expense of BTPE. The drastic reduction in BLE after 12 h of RI shows rapid moisture consumption. In the case of Yaas, there is a slight increase in BLE before IP,

and it deceased up to mid of IP, then it increased with nearly no change in BTPE.

Figure 9(c, g) shows the KE budget terms, namely KGEN (red), KDIS (black), and KFLX (blue). KGEN represents a constant production of BKE, KDIS represents its
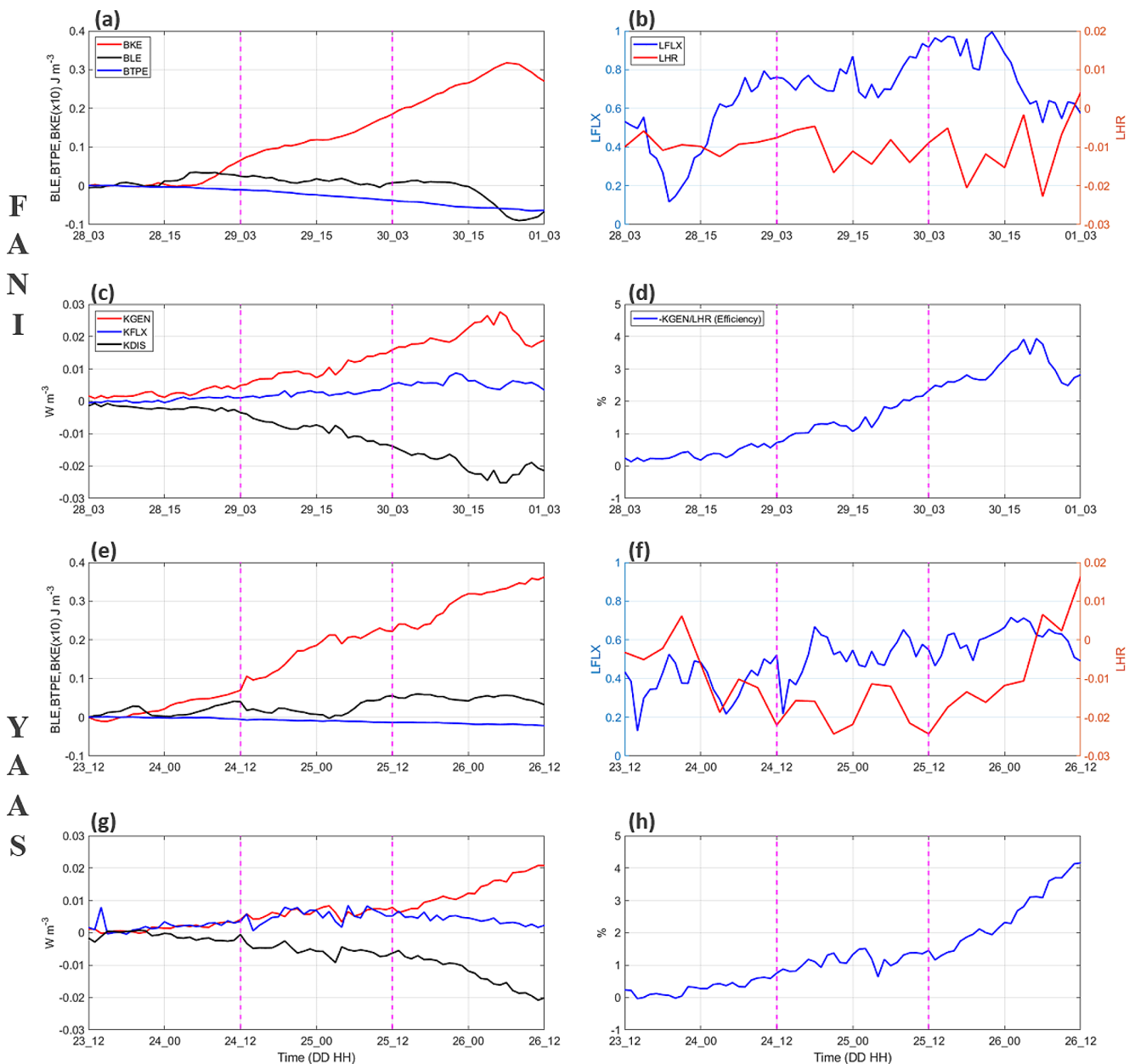
Fig. 9 (**a**) Volume integrated (J.m^{-3}) time series of BLE, BTPE, and BKE following the tropical cyclone Fani and the values are normalized with respect to the initial value at 12 h to make zero as the refer-ence point. Volume-averaged budget terms are presented in (**b**) for LE (W·m^{-3}), and (**c**) for KE (W·m^{-3}), (**d**) the efficiency of KGEN. (**e-h**) are the same as (**a-d**) but for Yaas

dissipation, and KFLX represents its flux divergence. The PBL friction (KDIS) and BKE production (KGEN) have significant offsets. The increasing (decreasing) trend of KGEN (KDIS) during the IP phase shows the steady generation of BKE and weak dissipation of KDIS. The slight increase in the KFLX shows the limited import of BKE through the lateral boundaries of the control volume.

Figure 9(b, f) shows the latent energy (LE) budget. The moisture supply is denoted as LFLX, while the moisture consumption is represented by LHR. There is an observed rise in the LFLX (>0.8 Wm^{-3}), accompanied by a minor

decline in the latent heat release (LHR). These fluctuations indicate a persistent accumulation of moisture within the control volume, while the rate of moisture consumption remains relatively stable. The observed simultaneous increase in BKE and KGEN indicates that the dynamical process is more influential than the thermodynamic process in the case of Fani.

The generation of KE takes place due to the conversion of LE through TPE. The major contributors to this energy conversion process are LHR and KGEN. Thus the analysis shown in Fig. 9 (d, h) accurately depicts the modulation

process of the thermodynamic efficiency (-KGEN/LHR). It is noted that only about 4% of LHR is converted into KE through KGEN shows that tropical cyclones are thermodynamically insufficient. The increase in efficiency is up to the increase of KGEN. It implies that in the weaker stage, TC is the least efficient in converting LE into KE.

Conclusion

In this study, the WRF model is used to understand the characteristic features, dynamics, and thermodynamics of an intensification of pre-monsoon cyclones over BoB. The study is being carried out for two pre-monsoon two TCs i.e. RI cyclone Fani and non-RI cyclone Yaas as they have significant intensification. The forecast is initialized at 1200 UTC on 27 April 2019 and 0000 UTC on 23 May 2021 for Fani and Yaas, respectively. The forecast results are validated against IMD's best track data. Both forecasts were able to capture the IP reasonably well; therefore, they are used for further analysis.

The 24-hour composite was plotted to understand the wind and specific humidity pattern around the vortex at a 180 km radius from the center. The composites were made for three phases pre-intensification (IP-24), Intensification (IP), and post-intensification (IP+24). At pre-intensification, in the case of Fani, wind speed reached up to 58 kts in the southern sector, while in the case of Yaas, the wind speed was low and nearly uniform around the vortex. During the intensification phase, the wind reached up to 88 knots in the southeastern quadrant for Fani, while the maximum wind was 76 knots for Yaas and extended from the southeastern to the southwestern quadrant. After IP, the maximum wind for Fani, located in the southeastern sector about 100 kts while for Yaas speed went up to 82 knots. Before, during, and especially after the intensification period, the MSLP in Fani and Yaas was remarkably consistent with one another. The circular and regular shape of the cyclone is revealed by the distribution pattern of SLP in Fani, which indicates that the cyclone was a highly structured system. In Fani, areas with high specific humidity were concentrated closer to the center of the region, whereas in Yaas, these areas were virtually uniformly distributed radially about the center and did not display any specific pattern.

The study compares the behaviour of two cyclones, Fani and Yaas, in terms of hydrometeors (cloud water, rainwater, cloud ice, snow, and graupel) and diabatic heating during the intensification phase. Fani showed a sharp increase in hydrometeors and diabatic heating before intensification, contributing to its RI, while Yaas remained stagnant. The intensification of Fani was significantly influenced by the increase in diabatic heating, whereas the impact of diabatic heating on the intensification of Yaas was comparatively less pronounced. Further analysis showed that in both cyclones, frozen and liquid hydrometeors, and diabatic heating were more concentrated on the western side of the cyclone. Fani had more hydrometeors in the eyewall region than the core region, which may have contributed to its intensification. The heating was more widespread and intense in the inner eyewall region than the core in Fani, while in Yaas, there was not much heating in the inner eyewall region with respect to the core region.

Prior to Fani's RI, there was a sudden increase in the rate of moisture convergence, which led to the formation of more cloud ice and the release of more latent energy. In contrast, the lack of moisture convergence in Yaas resulted in a weaker updraft, lesser transportation of liquid hydrometeors to upper levels, and a decrease in latent heat release. The increase in cloud water, decrease in graupel, and nearly constant snow and cloud ice in Yaas's intensification phase indicate the lack of transport of cloud water to upper levels, resulting in mostly warm rain processes. After the RI period of Fani, the MFC decreased, along with the rain rate and frozen hydrometeors, indicating the importance of a high moisture convergence rate for rapid intensification of TC.

The relationship between kinetic energy (KE) and latent energy (LE) budgets in two tropical cyclones, Fani and Yaas, is investigated. The results demonstrate that the change in bulk kinetic energy (BKE) is closely related to the change in cyclone intensity. During the intensification phase, the KE budget terms, including BKE production (KGEN), dissipation (KDIS), and flux divergence (KFLX), indicate constant BKE production and moderate dissipation. The LE budget parameters, which include moisture supply (LFLX) and consumption (LHR), indicate a continuous accumulation of moisture with a nearly constant moisture consumption. The low conversion efficiency of LE to KE through KGEN (approximately 4%) indicates that TCs are thermodynamically insufficient. The study emphasizes the predominance of dynamical processes over thermodynamic processes in the intensification of TCs.

Author contribution Pankaj Lal Sahu: Model simulations, Visualization, Coding, Result Interpretation, Manuscript Writing and Editing. Sandeep Pattnaik: Conceptualization, Result interpretation and Discussions, Manuscript Writing and Editing. Prasenjit Rath: Results interpretation and Discussions.

Declarations

Conflict of Interest The authors declared that they have no conflict of interest.

References

Baisya, H., Pattnaik, S., & Chakraborty, T. (2020). A coupled modeling approach to understand ocean coupling and energetics of tropical cyclones in the Bay of Bengal basin. *Atmos Res Art*, 105092. https://doi.org/10.1016/j.atmosres.2020.105092.

Banacos, P. C., & Schultz, D. M. (2005). The use of moisture flux convergence in forecasting convective initiation: Historical and operational perspectives. *Wea Forecasting*, 3, 351–366. https://doi.org/10.1175/waf858.1.

Cangialosi, J. P., Blake, E., DeMaria, M., Penny, A., Latto, A., Rappaport, E., & Tallapragada, V. (2020). Recent progress in Tropical Cyclone intensity forecasting at the National Hurricane Center. *Wea Forecasting*, 5, 1913–1922. https://doi.org/10.1175/waf-d-20-0059.1.

Chakraborty, T., Pattnaik, S., Jenamani, R. K., & Baisya, H. (2021). Evaluating the performances of cloud microphysical parameterizations in WRF for the heavy rainfall event of Kerala (2018). *Meteorology and Atmospheric Physics*, 3, 707–737. https://doi.org/10.1007/s00703-021-00776-3.

Duan, W., Yuan, J., Duan, X., & Feng, D. (2021). Seasonal Variation of Tropical Cyclone Genesis and the related large-scale environments: Comparison between the Bay of Bengal and Arabian Sea sub-basins. *Atmosphere*, 12(12), 1593. https://doi.org/10.3390/atmos12121593.

Dudhia, J. (1989). Numerical study of convection observed during winter monsoon experiment using a mesoscale two-dimensional model. *Journal of Atmospheric Science*, 46, 3077–3107.

Dutton, J. A. (1976). *The ceaseless wind*. McGraw-Hill Companies.

Hersbach, H., Bell, B., Berrisford, P., Biavati, G., Horányi, A., Muñoz Sabater, J., Nicolas, J., Peubey, C., Radu, R., Rozum, I., Schepers, D., Simmons, A., Soci, C., Dee, D., & Thépaut, J-N. (2023). : ERA5 hourly data on single levels from 1940 to present. Copernicus Climate Change Service (C3S) Climate Data Store (CDS), https://doi.org/10.24381/cds.adbb2d47.

Hogsett, W., & Zhang, D. L. (2009). Numerical Simulation of Hurricane Bonnie (1998). Part III: Energetics. *Journal of Atmospheric Science*, 9, 2678–2696. https://doi.org/10.1175/2009jas3087.1.

Hong, S-Y., Ying, N., & Dudhia, J. (2006). A new vertical diffusion with an explicit treatment of entrainment process. *Mon Wea Rev*, 134, 2318–2341. https://doi.org/10.1175/MWR3199.1.

Ito, K. (2016). Errors in Tropical Cyclone Intensity Forecast by RSMC Tokyo and statistical correction using environmental parameters. *SOLA*, 0, 247–252. https://doi.org/10.2151/sola.2016-049.

Kain, J. S. (2004). The Kain-Fritsch convective parameterization: An update. *Journal of Applied Meteorology*, 43, 170–181.

Kaplan, J., & DeMaria, M. (2003). Large-Scale Characteristics of Rapidly Intensifying Tropical Cyclones in the North Atlantic Basin. *Wea Forecasting*, 6, 1093–1108. https://doi.org/10.1175/1520-0434(2003)018<1093:lcorit>2.0.co;2.

Kaplan, J., DeMaria, M., & Knaff, J. A. (2010). A revised Tropical Cyclone Rapid Intensification Index for the Atlantic and Eastern North Pacific basins. *Wea Forecasting*, 1, 220–241. https://doi.org/10.1175/2009waf2222280.1.

Kaplan, J., Rozoff, C. M., DeMaria, M., Sampson, C. R., Kossin, J. P., Velden, C. S., Cione, J. J., Dunion, J. P., Knaff, J. A., Zhang, J. A., Dostalek, J. F., Hawkins, J. D., Lee, T. F., & Solbrig, J. E. (2015). Evaluating Environmental Impacts on Tropical Cyclone Rapid Intensification Predictability Utilizing Statistical Models. *Wea Forecasting*, 5, 1374–1396. https://doi.org/10.1175/waf-d-15-0032.1.

Lee, C. Y., Tippett, M. K., Sobel, A. H., & Camargo, S. J. (2016). Rapid intensification and the bimodal distribution of tropical cyclone intensity. *Nature Communications*, 1. https://doi.org/10.1038/ncomms10625.

Li, Y., Tang, Y., Wang, S., Toumi, R., Song, X., & Wang, Q. (2023). Recent increases intropical cyclone Rapid intensification events in global offshore regions. Nat. Commun 1. https://doi.org/10.1038/s41467-023-40605-2.

Lim, K. S. S., & Hong, S. Y. (2010). Development of an effective double-moment Cloud Microphysics Scheme with Prognostic Cloud condensation nuclei (CCN) for Weather and Climate models. *Mon Wea Rev*, 5, 1587–1612. https://doi.org/10.1175/2009mwr2968.1.

Liu, J., Zhang, F., & Pu, Z. (2017). Numerical simulation of the rapid intensification of Hurricane Katrina (2005): Sensitivity to boundary layer parameterization schemes. *Advances in Atmos Sci*, 4, 482–496. https://doi.org/10.1007/s00376-016-6209-5.

Mlawer, E. J., Steven, J. T., Patrick, D. B., Lacono, M. J., & Clough, S. A. (1997). Radiative transfer for inhomogeneous atmospheres: RRTM, a validated correlated k-model for the longwave. *Journal Geophysical Research*, 102, 16663–16682. https://doi.org/10.1029/97JD00237.

National Centers for Environmental Prediction/National Weather Service/NOAA/U.S. Department of Commerce. (2015). NCEP GDAS/FNL 0.25 degree global tropospheric analyses and Forecast Grids. *Research Data Archive at the National Center for Atmospheric Research Computational and Information Systems Laboratory*. https://doi.org/10.5065/D65Q4T4Z.

Nekkali, Y. S., Osuri, K. K., Das, A. K., & Niyogi, D. (2022). Understanding the characteristics of microphysical processes in the rapid intensity changes of tropical cyclones over the Bay of Bengal. *Quarterly Journal Royal Meteorological Society*, 749, 3715–3729. https://doi.org/10.1002/qj.4384.

Paulson, C. A. (1970). The mathematical representation of wind speed and temperature profiles in the unstable atmospheric surface layer. *Journal of Applied Meteorology*, 9, 857–861.

Rai, D., & Pattnaik, S. (2018). Sensitivity of Tropical Cyclone intensity and structure to Planetary Boundary Layer parameterization. *Asia Pac J Atmos Sci*, 3, 473–488. https://doi.org/10.1007/s13143-018-0053-8.

Rai, D., Pattnaik, S., & Rajesh, P. V. (2016). Sensitivity of tropical cyclone characteristics to the radial distribution of sea surface temperature. *Journal of Earth System Science*, 4, 691–708. https://doi.org/10.1007/s12040-016-0687-9.

Rappaport, E. N., Jiing, J. G., Landsea, C. W., Murillo, S. T., & Franklin, J. L. (2012). The Joint Hurricane Test Bed: Its First Decade of Tropical Cyclone Research-To-Operations Activities Reviewed. *Bulletin Of The American Meteorological Society*, 3, 371–380. https://doi.org/10.1175/bams-d-11-00037.1.

Trivedi, D., Pattnaik, S., & Joseph, S. (2023). Influence of coastal land–water–atmosphere interactions on tropical cyclone intensity over the Bay of Bengal. *Meteorology and Atmospheric Physics*, 135, 25. https://doi.org/10.1007/s00703-023-00964-3.

Vishwakarma, V., & Pattnaik, S. (2022). Role of large-scale and microphysical precipitation efficiency on rainfall characteristics of tropical cyclones over the Bay of Bengal. *Natural Hazards*, 114, 1585–1608. https://doi.org/10.1007/s11069-022-05439-z.

World Meteorological Organization. (2008). *Tropical cyclone operational plan for the Bay of Bengal and the Arabian Sea* (pp. TCP–21). Document No. WMO/TD No. 84.

Wu, S. N., Soden, B. J., & Alaka, G. J. (2020). Ice Water Content as a Precursor to Tropical Cyclone Rapid Intensification. *Geophysical Reseach Letters*, 21. https://doi.org/10.1029/2020gl089669.

Yanai, M., Esbensen, S., & Chu, J. H. (1973). Determination of Bulk properties of Tropical Cloud clusters from large-scale heat and moisture budgets. *Journal of Atmospheric Science*, *4*, 611–627. https://doi.org/10.1175/1520-0469(1973)030<0611:dobpot>2.0.co;2.

Zhao, D., Yu, Y., Yin, J., & Xu, H. (2020). Effects of Microphysical Latent Heating on the Rapid Intensification of Typhoon Hato (2017). *J Meteorol Res*, *2*(368-386). https://doi.org/10.1007/s13351-020-9076-z.